ELSEVIER

Soil Dynamics and Earthquake Engineering 22 (2002) 191–204

SOIL DYNAMICS AND EARTHQUAKE ENGINEERING

www.elsevier.com/locate/soildyn

Plasticity model for sand under small and large cyclic strains: a multiaxial formulation

Achilleas G. Papadimitriou*, George D. Bouckovalas

Department of Geotechnical Engineering, Faculty of Civil Engineering, National Technical University of Athens, 42 Patission Street, 10682 Athens, Greece

Accepted 23 November 2001

Abstract

This paper presents the multiaxial formulation of a plasticity model for sand under cyclic shearing. The model adopts a kinematic hardening circular cone as the yield surface and three non-circular conical surfaces corresponding to the deviatoric stress ratios at phase transformation, peak strength and critical state. The shape of the non-circular surfaces is formulated in accordance with the experimentally established failure criteria, while their size is related to the value of the state parameter ψ. To simulate cyclic response under small and large shear strain amplitudes without a change in model parameters, it was found necessary to introduce: (a) a non-linear hysteretic (Ramberg–Osgood type) formulation for the strain rate of elastic states and (b) an empirical index of the effect of fabric evolution during shearing which scales the plastic modulus. This index is estimated in terms of a macroscopic second-order fabric tensor, which develops as a function of the plastic volumetric strain increment and the loading direction in the deviatoric plane. Comparison of simulations to pertinent data from 27 resonant column, cyclic triaxial and cyclic direct simple shear tests provide a measure for the overall accuracy of the model.

Keywords: Bounding surface; Constitutive equations; Critical state; Cyclic loading; Fabric; Hysteresis; Liquefaction; Sand; State parameter

1. Introduction

Traditionally, the ability to simulate cyclic shearing in an elasto-plastic context has been addressed by incorporating kinematic hardening [24] and by appropriately modifying the flow rule, otherwise designed and calibrated for monotonic shearing. In this manner, some basic elements of cyclic shearing, such as stiffness degradation and hysteretic energy dissipation (damping), can be simulated in a qualitative rather than a quantitative manner. However, simulating cyclic shearing in practice is far more demanding, since it must also address various other issues, such as strain accumulation or excess pore pressure buildup, and all these with quantitative accuracy. In fact, any pertinent analytical simulation should be able to address the full spectrum of cyclic response, which is primarily a function of the amplitude of the cyclic shear strain γ_c [8,14,32]. Moreover, for numerical applications, it is imperative that the model applies for multiaxial shearing of various γ_c levels and initial (density and stress) conditions with a single set of parameters.

The effect of initial conditions on sand response has been effectively accounted for in the literature by incorporating the state parameter ψ in constitutive equations, either implicitly [16] or explicitly [10,19,21,34]). To account for the effect of γ_c, Papadimitriou et al. [27] recently presented a development of the model of Manzari and Dafalias [21], where: (a) a non-linear hysteretic (Ramberg–Osgood type) formulation was adopted for elastic states and (b) an empirical estimator of the effect of fabric evolution during shearing was introduced to scale the magnitude of plastic strains. The new model was initially formulated for triaxial testing conditions. Hence, the constitutive equations were presented in terms of the triaxial deviatoric stress $q = \sigma_v - \sigma_h$ and the mean effective stress $p = (\sigma_v + 2\sigma_h)/3$, where subscripts v and h denote the vertical and the horizontal directions, respectively. The triaxial testing conditions are a special case of shearing, which provide simplicity in the presentation of constitutive equations of the model and enable elaboration on how it was formulated and calibrated in accordance with the experimental data.

This paper presents a multiaxial formulation of the aforementioned model, which is necessary for the implementation

* Corresponding author. Tel.: +30-10-7723-744/+30-10-8238-183; fax: +30-10-7723-428.

E-mail addresses: loupapas@alum.mit.edu (A.G. Papadimitriou), g.bouck@civil.ntua.gr (G.D. Bouckovalas).

0267-7261/02/$ - see front matter
PII: S0267-7261(02)00009-X

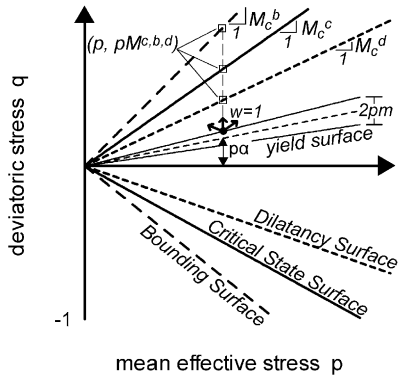

Fig. 1. Model surfaces in the [q–p] triaxial stress space—definition of mobilized deviatoric stress ratios $M^{c,b,d}$ (projection rule).

of the model in numerical codes used for solving general boundary value problems of geotechnical earthquake engineering. A special emphasis is given to the generalizing scheme, and more specifically to the assumption concerning the effect of the intermediate principal stress σ_2, as this stems from experimental evidence. Furthermore, the empirical index of the effect of fabric evolution is improved to account for the directivity of multiaxial shearing by means of a second-order tensor. The overall performance of the model is evaluated in comparison to measurements from 27 resonant column, cyclic triaxial and cyclic direct simple shear tests performed on Nevada sand [2].

In the following, tensorial quantities are denoted by boldface characters (e.g. $\boldsymbol{\sigma}$ denotes the effective stress tensor), so that they can be readily distinguished from plain text scalars.

2. Basic concepts and equations

The proposed elasto-plastic formulation is a yield/bounding surface critical state model, formulated in terms of effective stresses. Hence, it adopts a unique Critical State Surface (CSS) in the [$\boldsymbol{\sigma}$–void ratio e] space, which is independent of the sample preparation method (i.e. depositional anisotropy), the shear path direction and the drainage conditions. The projection of the CSS on the [e–ln(p)] space is assumed linear and is named critical state line (CSL). Consequently, the state parameter ψ of Been and Jefferies [4] is given as:

$$\psi = e - e_{cs} = e - (e_{cs})_a + \lambda \ln(p/p_a), \tag{1}$$

where $(e_{cs})_a$ and λ are user-defined parameters, while p_a is the atmospheric pressure in the desired units (e.g. p_a = 98.1 kPa in SI). The form given to e_{cs} in Eq. (1) is the simplest possible, since it requires the calibration of merely two constants. Other forms could be used in variants of this model, without further changes in constitutive equations.

For simplicity, the shape and the role of model surfaces is first described in the triaxial [q–p] stress space with the aid of Fig. 1. Observe that the model is characterized by an open wedge-type yield surface with the following yield function [21]:

$$f = \eta - \alpha \mp m = \eta - \alpha - wm = 0, \tag{2}$$

where η is the deviatoric stress ratio q/p at yield. The values of α and m correspond to tangents of angles related to the bisector and the opening of the yield surface. While m remains constant (no isotropic hardening), α is the kinematic hardening variable.

The $\mp$ sign is alternatively included in Eq. (2) via parameter w, i.e. the 'direction' of triaxial shearing. This name stems from the fact that $w = +1$ for shearing in triaxial compression (where $\sigma_1 > \sigma_2 = \sigma_3$) and $w = -1$ for shearing in triaxial extension ($\sigma_1 = \sigma_2 > \sigma_3$). In this way, $\eta = (\alpha + m)$ when yielding is reached in compression (i.e. $f = 0$ for $w = +1$), while $\eta = (\alpha - m)$ when yielding is reached in extension (i.e. $f = 0$ for $w = -1$). Hence, knowledge of α is mandatory for defining the value of the mobilized deviatoric stress ratio η at yield. This means that the deviatoric stress ratio-valued parameter α is essentially a state variable associated with the recent stress–strain history. In plasticity literature, state variables such as α are referred to as back-stress ratios.

Furthermore, the model incorporates three additional open wedge-type surfaces with apex at the origin of stress space: the critical state surface, the bounding surface and the dilatancy surface. As shown in Fig. 1, their shape for triaxial compression is uniquely defined by the deviatoric stress-ratios M_c^c, M_c^b and M_c^d, respectively, or $M_c^{c,b,d}$, collectively. In the same manner, deviatoric stress-ratios $M_e^{c,b,d}$ define the shapes of these surfaces for triaxial extension. Based on Manzari and Dafalias [21], who extended the work of Wood et al. [34], these deviatoric stress-ratios are interrelated by:

$$M_{c,e}^b = M_{c,e}^c + k_{c,e}^b \langle -\psi \rangle \tag{3a}$$

$$M_{c,e}^d = M_{c,e}^c + k_{c,e}^d \psi \tag{3b}$$

where $\langle\ \rangle$ are the Macauley brackets yielding $\langle A \rangle = A$ if $A > 0$ and $\langle A \rangle = 0$ if $A \le 0$. The parameters k_c^b and k_c^d are positive constants, while the critical state deviatoric stress ratios M_c^c and M_e^c are user-defined independent parameters.

As a first approximation for practical applications, it is assumed that:

$$k_e^{b,d} = (M_e^c/M_c^c) k_c^{b,d} \tag{4}$$

Nevertheless, for greater accuracy, this interrelation can be omitted at the cost of two extra parameters (k_e^b and k_e^d).

Along the lines of bounding surface plasticity [7], the critical state, the bounding and the dilatancy surfaces can be viewed as the loci of the respective 'image' points of the current stress state. An example definition of image points according to the adopted projection rule is provided in Fig. 1. Observe that, for all compressive stress rates (like the ones denoted by vectors in Fig. 1), the image points of

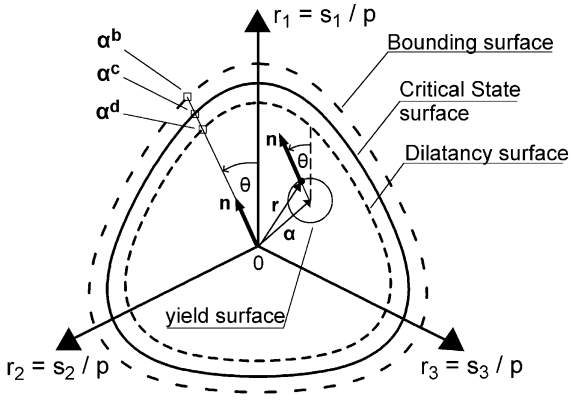

Fig. 2. Model surfaces in the multiaxial stress space—definition of conjugate deviatoric back-stress ratio tensors $\boldsymbol{\alpha}^{c,b,d}$ (projection rule).

$[p, q(=p\eta)]$ on the three surfaces are points $[p, w(pM^{c,b,d})]$, where:

$$M^{c,b,d} = M_c^{c,b,d}\langle w\rangle + M_e^{c,b,d}\langle -w\rangle \tag{5}$$

In this way, the image of $[p, q]$ is point $[p, pM_c^{c,b,d}]$ for $w = 1$ (Fig. 1) and point $[p, -pM_e^{c,b,d}]$ for $w = -1$. Given this projection rule, the scalar 'distances' $d^{c,b,d}$ of the current stress state from the three model surfaces are defined as $d^{c,b,d} = (M^{c,b,d} - w\eta)$, i.e. in terms of deviatoric stress ratios.

According to Eq. (2), $\alpha = \eta - wm$, hence, η and α are constantly interrelated. Similarly, one may relate the deviatoric stress ratios $M^{c,b,d}$ of Eq. (5) to the respective deviatoric stress ratio-valued parameters $\alpha^{c,b,d}$ according to:

$$\alpha^{c,b,d} = M^{c,b,d} - m, \tag{6}$$

where $\alpha^{c,b,d}$ correspond to the respective conjugate values of the current deviatoric stress ratio-valued parameter α (or conjugate back-stress ratios on the three surfaces). Given this definition, the three surfaces can be alternatively viewed as the loci of $\alpha^{c,b,d}$ values. In this approach, the scalar distances $d^{c,b,d}$ are redefined as $d^{c,b,d} = (\alpha^{c,b,d} - w\alpha)$, i.e. in terms of deviatoric stress ratio-valued parameters. For triaxial testing conditions, these two definitions of model surfaces and scalar distances $d^{c,b,d}$ are analytically equivalent and none is preferable to the other. In the multiaxial stress space, the latter is preferred for reasons that will be discussed in Section 3.

The general form of the stress–strain relations is that of classical elasto-plasticity. Namely, the total strain rate $\mathbf{d}\varepsilon$ is deconvoluted into an elastic component $\mathrm{d}\boldsymbol{\varepsilon}^{\mathrm{e}}$ and a plastic component $\mathrm{d}\boldsymbol{\varepsilon}^{\mathrm{p}}$. If $\mathbf{e}$ and $\mathbf{s}$ denote the deviatoric strain and stress tensors, then the elastic deviatoric and volumetric strain rates are given by:

$$\boldsymbol{d}\mathbf{e}^{\mathrm{e}} = \frac{d\mathbf{s}}{2G_{\mathrm{t}}} \tag{7a}$$

$$\mathrm{d}\varepsilon_{\mathrm{p}}^{\mathrm{e}} = \frac{\mathrm{d}p}{K_{\mathrm{t}}}, \tag{7b}$$

where G_{t} and K_{t} are the tangential elastic shear and bulk moduli, respectively. In turn, the plastic strain rate is given by the following general equation:

$$\mathrm{d}\boldsymbol{\varepsilon}^{\mathrm{p}} = \langle\Lambda\rangle\mathbf{R}, \tag{8}$$

where tensor $\mathbf{R}$ defines the direction of the plastic strain rate and Λ is the scaling loading index, given by:

$$\Lambda = \frac{\mathbf{L} : \mathrm{d}\boldsymbol{\sigma}}{K_{\mathrm{p}}}, \tag{9}$$

where K_{p} is the plastic modulus and $\mathbf{L} = \partial f/\partial\boldsymbol{\sigma}$ is the normal to the yield surface defining the loading direction in multiaxial stress space. Note that the operator : between two tensorial quantities denotes the double inner product of these tensors and provides the trace of their product. The inclusion of the Macauley brackets in Eq. (8) ensures that non-positive values of Λ lead to $d\boldsymbol{\varepsilon}^{\mathrm{p}} = 0$. In other words, it is the sign of Λ that distinguishes loading ($\Lambda > 0$), from unloading ($\Lambda < 0$) or neutral loading ($\Lambda = 0$).

Eqs. (7a) through (9) provide a general outline of the proposed incremental stress–strain relations in multiaxial space. Full presentation of the model requires specific analytical expressions for the model surfaces, the elastic moduli G_{t} and K_{t}, the plastic modulus K_{p} and the plastic strain direction tensor $\mathbf{R}$. These issues are in turn the subjects of the following paragraphs.

3. Model surfaces in multiaxial stress space

The open wedge-type surfaces of the model in triaxial testing conditions become open cones in the multiaxial stress space. Hence, the surfaces are fully defined in terms of the deviatoric stress ratio tensor $\mathbf{r} = \mathbf{s}/p$. In particular, of importance is merely the cross-section of these surfaces on the π-plane of the $\mathbf{r}$ space, i.e. the plane perpendicular to the diagonal of this space.

The yield surface of the model is given the shape of a kinematically hardening circular cone with apex at the origin of axes, expressed as [21]:

$$f = \sqrt{(\mathbf{s} - p\boldsymbol{\alpha}) : (\mathbf{s} - p\boldsymbol{\alpha})} - \sqrt{2/3}mp = 0, \tag{10}$$

where $\boldsymbol{\alpha}$ is a deviatoric stress ratio-valued tensor, which determines the axis of the circular cone with radius equal to $\sqrt{2/3}m$. The role of tensor $\boldsymbol{\alpha}$ in multiaxial stress space is the same as scalar α in the triaxial space, i.e. it is a deviatoric back-stress ratio tensor. Among other issues, Fig. 2 shows the circular shape of the yield surface on the π-plane of the $\mathbf{r}$ space. The normal to the yield surface, denoted by tensor $\mathbf{L}$ in Eq. (9), is now given by:

$$\mathbf{L} = \mathbf{n} - \frac{V}{3}\mathbf{I} \tag{11a}$$

where:

$$\mathbf{n} = \frac{\mathbf{r} - \boldsymbol{\alpha}}{\sqrt{2/3}m} \tag{11b}$$

$$V = \boldsymbol{\alpha} : \mathbf{n} + \sqrt{2/3}m \tag{11c}$$

Tensor $\mathbf{I}$ is the second order identity tensor and $\mathbf{n}$ is the unit deviatoric stress ratio tensor ($\mathbf{n} : \mathbf{n} = 1$). As deduced from Fig. 2 and Eqs. (11a)–(11c), tensor $\mathbf{n}$ is the component of the loading direction $\mathbf{L}$ that lies on the π-plane of the $\mathbf{r}$ space. As mentioned in Section 2, the model does not incorporate isotropic hardening. Hence, its size, quantified by scalar m, remains fixed to a value that should lead to a relatively small, but distinguishable for numerical purposes, yield surface. Application of the model has shown that a value of $m = 0.06$–0.07 meets these requirements. Note that the circular shape given to the yield surface on the π-plane is the simplest possible, since Eq. (10) does not include any type of dependence on a Lode angle θ or on third invariants of stresses. Any other, possibly more accurate, shape would have complicated the form of the loading direction $\mathbf{L}$, since it would have to include derivatives of function f with respect to θ and derivatives of θ with respect to $\boldsymbol{\sigma}$, with possibly small benefits in overall accuracy (e.g. [10]).

The critical state, the bounding and the dilatancy surfaces are also conical, but are not characterized by a circular shape on the π-plane, since $M_{\mathrm{c}}^{c,b,d} \neq M_{\mathrm{c}}^{c,b,d}$ and equivalently, $\boldsymbol{\alpha}_{\mathrm{c}}^{c,b,d} \neq \boldsymbol{\alpha}_{\mathrm{e}}^{c,b,d}$, in general. In their case, the model requires the calculation of Lode angle θ, which is defined in terms of the stress ratio tensor $\bar{\mathbf{r}} = \mathbf{r} - \boldsymbol{\alpha}$ (e.g. [11,21]) according to:

$$\cos(3\theta) = \frac{3\sqrt{3}}{2}\frac{\bar{J}_3}{\bar{J}_2^{3/2}}, \tag{12}$$

where $\bar{J}_2 = (1/2)\bar{\mathbf{r}} : \bar{\mathbf{r}}$ and $\bar{J}_3 = (1/3)\bar{\mathbf{r}} : \bar{\mathbf{r}} : \bar{\mathbf{r}}$ are the second and third invariants of stress ratio tensor $\bar{\mathbf{r}}$. The Lode angle θ corresponds to the direction of the stress ratio tensor $\bar{\mathbf{r}}$ (or equivalently of $\mathbf{n}$) on the π-plane (Fig. 2) and varies from $\theta = 0$ for triaxial compression to $\theta = \pi/3$ for triaxial extension.

As shown in Fig. 2, model surfaces in the multiaxial stress space are defined in terms of the conjugate deviatoric (back) stress ratio-valued tensors $\boldsymbol{\alpha}^{c,b,d}$ corresponding to the three surfaces, as [21]:

$$\boldsymbol{\alpha}^{c,b,d} = \sqrt{2/3}\alpha_\theta^{c,b,d}\mathbf{n}, \tag{13}$$

where $\alpha_\theta^{c,b,d}$ are continuous deviatoric stress ratio-valued functions of angle θ taking the values $\alpha_0^{c,b,d} = \alpha_{\mathrm{c}}^{c,b,d}$ ($= M_{\mathrm{c,e}}^{c,b,d} - m$) for triaxial compression ($\theta = 0$), $\alpha_{\pi/3}^{c,b,d} = \alpha_{\mathrm{e}}^{c,b,d}$ ($= M_{\mathrm{e}}^{c,b,d} - m$) for triaxial extension ($\theta = \pi/3$) and intermediate values for non-triaxial conditions ($0 < \theta < \pi/3$). In other words, Eq. (13) corresponds to the projection rule of the model in the multiaxial stress space. Given this projection rule, the scalar distances $d^{c,b,d}$ are defined as:

$$d^{c,b,d} = (\boldsymbol{\alpha}^{c,b,d} - \boldsymbol{\alpha}) : \mathbf{n} \tag{14}$$

Note that while the three surfaces in the triaxial stress space are defined either in terms of $M_{\mathrm{c}}^{c,b,d}$ or in terms of $\alpha_{\mathrm{c,e}}^{c,b,d}$ (see Section 2), their shape in the multiaxial stress space is uniquely defined in terms of $\alpha_{\mathrm{c,e}}^{c,b,d}$ (Eq. (13)). Similarly, in Eq. (14), it is the location of $\boldsymbol{\alpha}$ (i.e. a point on the π-plane) with respect to model surfaces that is of importance for the definition of scalar distances $d^{c,b,d}$. In the alternative case of defining model surfaces in the multiaxial stress space in terms of $M_{\mathrm{c,e}}^{c,b,d}$, the model would have to address how the kinematically hardening yield surface would eventually adjoin to the model surfaces, an issue that could be analytically complicated.

The generally non-circular shape of the critical state, the bounding and the dilatancy surfaces is introduced via the Lode angle θ dependence of scalars $\alpha_\theta^{c,b,d}$ in Eq. (13). These are defined as:

$$\alpha_\theta^{c,b,d} = g(\theta, c^{c,b,d})M_{\mathrm{c}}^{c,b,d} - m, \tag{15}$$

where $g(\theta, c^{c,b,d})$ is the function that introduces the effect of Lode angle θ and $c^{c,b,d} = M_{\mathrm{e}}^{c,b,d}/M_{\mathrm{c}}^{c,b,d}$ (≤ 1). In this way, the complicated task of defining model surfaces in terms of third invariants of stresses degenerates into merely defining an appropriate continuous function g in Eq. (15) with the following prerequisites: $g = 1$ for $\theta = 0$ and $g = c^{c,b,d}$ for $\theta = \pi/3$. The usual selection for this purpose is the well-known and established formula of Argyris et al. [1]:

$$g(\theta, c^{c,b,d}) = \frac{c^{c,b,d}}{\dfrac{(1 + c^{c,b,d})}{2} - \dfrac{(1 - c^{c,b,d})}{2}\cos(3\theta)} \tag{16}$$

In this paper, an alternative form for function g is proposed, which is based on Eq. (16), but yields more accurate strength predictions for non-triaxial conditions, namely:

$$g(\theta, c^{c,b,d}) = \frac{2c^{c,b,d}}{\left[\dfrac{(1 + c^{c,b,d})}{2} - \dfrac{(1 - c^{c,b,d})}{2}\cos(3\theta)\right] - \left[\dfrac{(1 + c^{c,b,d})}{2} + \dfrac{(1 - c^{c,b,d})}{2}\cos(3\theta)\right]} \tag{17}$$

When $c^{c,b,d} = 1$, both Eqs. (16) and (17) lead to circular cones centered at the hydrostatic axis (i.e. take the form of Drucker–Prager cones). An example of the shapes of the three surfaces on the π-plane, based on Eq. (17) with $c^{c,b,d} = 0.8$, is given in Fig. 2.

The accuracy of Eqs. (16) and (17) for non-triaxial conditions is explored parametrically in Fig. 3, where the friction angle φ is related to the intermediate principal stress parameter $b = (\sigma_2 - \sigma_3)/(\sigma_1 - \sigma_3)$ and the friction angle in triaxial compression $\varphi_{\mathrm{TC}} = \varphi$ (for $b = 0$). More specifically, the values of φ that procure by using Eqs. (16) and (17) (and demanding $d^{c,b,d} = 0$) are denoted as the 'Argyris et al.' and the 'proposed' failure criteria, respectively in Fig. 3. These predictions are compared to three well-known failure criteria, established on the basis of extensive experimental data: (a) Mohr-Coulomb, (b) Matsuoka and Nakai [22] and (c) Lade and Duncan [17]. Note that these

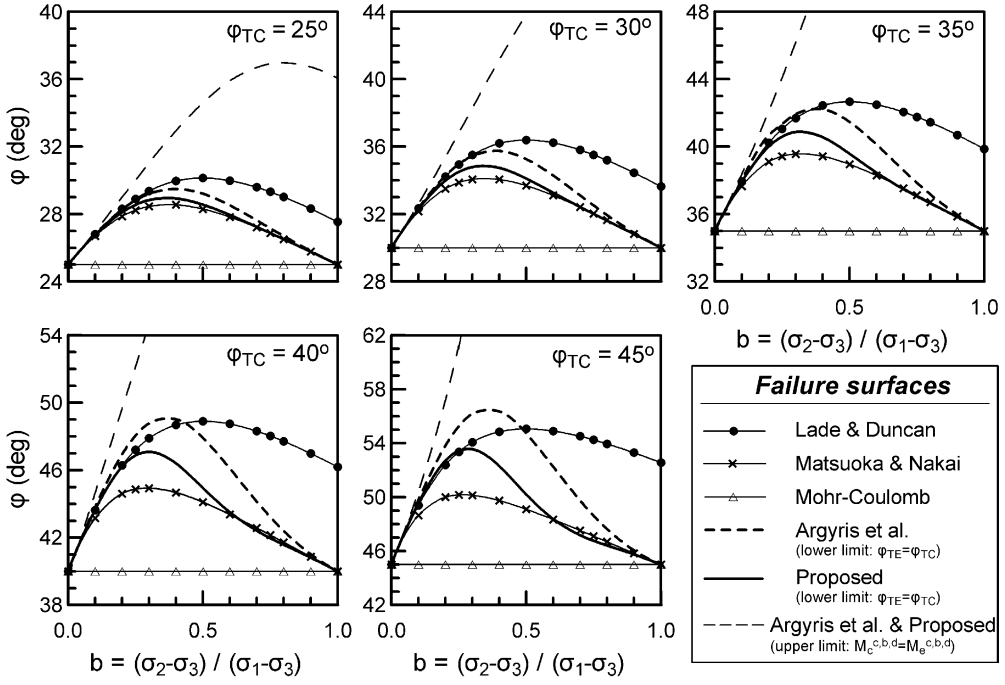

Fig. 3. Friction angle φ as a function of the b parameter, according to different failure criteria.

three criteria require only the value of φ_{TC} as input, while Eqs. (16) and (17) are defined as functions of both φ_{TC} and φ_{TT}. Hence, their respective estimates are shown for two extreme conditions:

$\varphi_{TE} = \varphi_{TC}$, that provides the lower limit of φ, and $\alpha_e^{c,b,d} = \alpha_c^{c,b,d}$ (or else $M_e^{c,b,d} = M_c^{c,b,d}$), that provides the (unlikely) upper limit.

Observe that if the upper limit condition is adopted, both Eqs. (16) and (17) seriously overestimate the φ values, but estimates are much better for the lower limit condition. Nevertheless, even for the lower limit condition, the 'Argyris et al.' relation still overestimates φ, for small b values ($b = 0.1$–0.5) and for large φ_{TC} values ($\varphi_{TC} \geq 35°$). This deficiency is clearly improved with Eq. (17) used in the proposed model.

4. Calculation of elastic strains

The elastic moduli K_t and G_t included in Eqs. (7a) and (7b) are interrelated via a constant elastic Poisson's ratio ν according to isotropic elasticity:

$$K_t = \frac{2(1+\nu)}{3(1-2\nu)} G_t \tag{18}$$

Furthermore, the tangential elastic shear modulus G_t is assumed to decrease smoothly from its maximum value G_{max} to its ever-current value G_t according to the following relation:

$$G_t = \frac{G_{max}}{T} \tag{19a}$$

where G_{max} is given by a generalization of the well-established formula of Hardin [12]:

$$G_{max} = \frac{B p_a}{0.3 + 0.7 e^2} \sqrt{\frac{p}{p_a}} \tag{19b}$$

The scalar parameter T (≥ 1) is a function of the variation in the value of the deviatoric stress ratio tensor $\mathbf{r}$ relative to its value $\mathbf{r}^{ref}$ at an appropriate reference state. This variation in tensor $\mathbf{r}$ is quantified with the aid of auxiliary scalar parameter $\chi_{\mathbf{r}}^{ref}$ given by:

$$\chi_{\mathbf{r}}^{ref} = \sqrt{1/2(\mathbf{r} - \mathbf{r}^{ref}) : (\mathbf{r} - \mathbf{r}^{ref})} \tag{20}$$

The model distinguishes two reference states: (a) the consolidation state for the first shearing path, where $\mathbf{r}^{ref} = \mathbf{r}^0$ and $\chi_{\mathbf{r}}^{ref} = \chi_{\mathbf{r}}^0$, and (b) the last shear reversal point (SR), where $\mathbf{r}^{ref} = \mathbf{r}^{SR}$ and $\chi_{\mathbf{r}}^{ref} = \chi_{\mathbf{r}}^{SR}$. Given these definitions, T is expressed as:

$$T = \left\{ \begin{array}{ll} 1 + \kappa\left(\frac{1}{a_1} - 1\right)\left(\frac{\chi_{\mathbf{r}}^0}{\eta_1}\right)^{\kappa-1}, & \text{first shearing} \\ 1 + \kappa\left(\frac{1}{a_1} - 1\right)\left(\frac{\chi_{\mathbf{r}}^{SR}}{2\eta_1}\right)^{\kappa-1}, & \text{after SR} \end{array} \right\}$$

$$\leq 1 + \kappa\left(\frac{1}{a_1} - 1\right), \tag{21}$$

where a_1 and η_1 are positive scalars, while κ is a constant

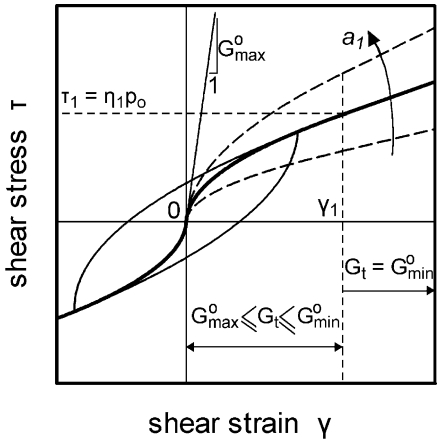

Fig. 4. Exemplary pure shear stress–strain [τ–γ] relation according to the proposed Ramberg–Osgood type shear formulation—effect of a_1.

that takes values ≥ 1. The simulations in this paper have been performed with $\kappa = 2$, i.e. the value of the fixed κ in the respective equation of Papadimitriou et al. [27]. Shear reversal (SR) is defined with the aid of scalar $\chi_{\mathbf{e}}^{\mathrm{SR}}$ where:

$$\chi_{\mathbf{e}}^{\mathrm{SR}} = \sqrt{1/2(\mathbf{e} - \mathbf{e}^{\mathrm{SR}}) : (\mathbf{e} - \mathbf{e}^{\mathrm{SR}})} \tag{22}$$

More specifically, SR is defined at a point where $\mathrm{d}\chi_{\mathbf{e}}^{\mathrm{SR}}$ changes sign. By and large, SR can occur for both elastic ($f < 0$) and plastic states ($f = 0$). Furthermore, a SR point is generally different from a point of loading reversal: from loading ($\Lambda > 0$) to unloading ($\Lambda < 0$) or neutral loading ($\Lambda = 0$).

Notice that Eqs. (19a) and (21) are reminiscent of the well-established one-dimensional hysteretic model of Ramberg and Osgood [29]. Besides hysteresis, the proposed elastic strain formulation produces small irreversible strains in closed shear stress cycles, due to the hypoelastic form of $G_{\max}$. As such, the proposed model does not have a region of true elastic behavior. According to Hueckel and Nova [13], a better term for such formulations is para-elastic. Nevertheless, the term 'elastic' strains is maintained in this paper to remind that the strains estimated by Eqs. (7a) and (7b) with the aid of Eqs. (18)–(22) apply to stress states within, as well as on the yield surface.

To gain insight to the proposed elastic formulation and to the role of parameters η_1 and a_1 in Eq. (21), one may assume pure shearing conditions, i.e. uni-directional τ–γ shearing under constant normal stresses and strains. In this simplified shearing case, $\chi_{\mathbf{r}}^{\mathrm{SR}} = |\tau - \tau^{\mathrm{SR}}|/p_{\mathrm{o}}$ and $\chi_{\mathbf{e}}^{\mathrm{SR}} = |\gamma - \gamma^{\mathrm{SR}}|/2$. Fig. 4 shows examples of the elastic stress–strain relation resulting for pure monotonic and cyclic shear, which is characterized by constant $G_{\max}(= G^0_{\max})$. As shown in this figure, model parameter a_1 governs the non-linearity procuring from the elastic strain formulation, namely a decrease of a_1 leads to increased non-linearity. More importantly, observe that the monotonic path for $\tau < \tau_1(= \eta_1 p_{\mathrm{o}})$ is characterized by a steadily decreasing G_{t}, while for $\tau \geq \tau_1$, the value of G_{t} remains constant and equal to $G^0_{\min} = G^0_{\max}/[1 + \kappa(1/a_1 - 1)]$. Under these simplifying assumptions, the elastic stress–strain relation may become analytically integratable (see Ref. [27] for the variant of the model with $\kappa = 2$). In this paper, the variable η_1 is related to a characteristic amplitude of shear strain γ_1 (a model parameter) according to:

$$\eta_1 = \frac{\tau_1}{p_{\mathrm{SR}}} = a_1 \left(\frac{G^{\mathrm{SR}}_{\max}}{p_{\mathrm{SR}}} \right) \gamma_1, \tag{23}$$

where $G^{\mathrm{SR}}_{\max}$ and p_{SR} are the values of the maximum shear modulus $G_{\max}$ and the mean effective stress p at the last SR, respectively. For the first shearing path in particular, $G^{\mathrm{SR}}_{\max} = G^0_{\max}$ and $p_{\mathrm{SR}} = p_{\mathrm{o}}$, i.e. variable η_1 is related to the values of $G_{\max}$ and p at consolidation.

Based on Eq. (23), variable η_1 becomes a measure of shear stress ratio tensor $\mathbf{r}$ variation related to shear strain amplitude γ_1, independent of stress and density conditions. Since $G_{\mathrm{t}} = G_{\min}$ for $\gamma \geq \gamma_1$, parameter γ_1 may be interpreted as a threshold strain beyond which any further degradation in the overall shear stiffness is due to the development of plastic shear strain. From an experimental point of view, Vucetic [32] found that irreversible strains become increasingly significant for cyclic shear strain amplitudes γ_{c} larger than the cyclic threshold shear strain γ_{tv} that varies between 6.5×10^{-5} and 2.5×10^{-4} for non-plastic sands and silts. Hence, γ_1 is physically associated to γ_{tv}.

5. Plastic strains and kinematic hardening

The direction of the plastic strain tensor $\mathbf{R}$ in Eq. (8) is given the following general form:

$$\mathbf{R} = \mathbf{n} + \frac{D}{3}\mathbf{I} \tag{24}$$

where D is a scalar parameter, named dilatancy coefficient. Observe that Eq. (24), which yields the direction of plastic strain $\mathbf{R}$, is very similar to Eq. (11a), which yields the loading direction $\mathbf{L}$. Obviously, if $\mathbf{R} = \mathbf{L}$, then the model would be characterized by an associated flow rule and a condition of $D = -V$ would apply. In the proposed model, the flow rule is non-associated and D takes the following form [21]:

$$D = A_{\mathrm{o}} d^d \tag{25}$$

where A_{o} is a positive model constant and d^d is the scalar distance from the dilatancy surface. Note that Eq. (25) is practically an efficient generalization of the flow rule of Nova and Wood [25], who first proposed an invariant form of the dilatancy theory of Rowe [30].

Eq. (24) implies that the value of D affects merely the volumetric component of the plastic strain rate $d\varepsilon^{\mathrm{p}}_{\mathrm{p}}$, while Eq. (25) shows that the sign of D depends solely on the sign of d^d. If, for example, loading ($\Lambda > 0$) continues beyond the dilatancy surface, then d^d and D become negative and

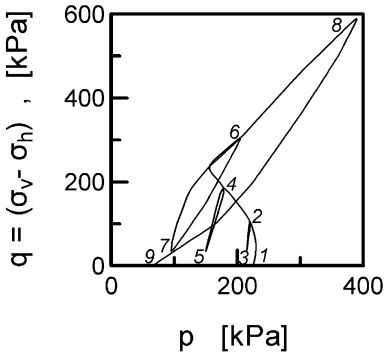

Fig. 5. Effective stress path of a typical undrained triaxial test including shear reversals (figure reproduced from Ref. [15]).

consequently the resulting $d\varepsilon_p^p$ becomes also negative, i.e. dilative behavior is simulated. In this sense, the dilatancy surface corresponds to the phase transformation line of Ishihara et al. [15]. Moreover, to ensure that no dilation occurs in the unlikely case of $\psi > 0$ and $d^d < 0$, a requirement of $D = 0$ is introduced until one of the two inequalities ceases to hold [21].

The plastic modulus K_p in Eq. (9) is related to the distance from the bounding surface d^b as:

$$K_p = p h_b h_f d^b \tag{26}$$

All parameters included in Eq. (26) are non-negative, except for d^b that essentially controls the sign of K_p. For instance, when the bounding surface of the model is crossed, then $d^b < 0$, and the post-peak strain softening behavior of dilative soils is initiated. Among the remaining parameters, scalar parameter h_f is an empirical macroscopic index of the effect of sand fabric evolution during shearing, which is presented in Section 6 that follows, while:

$$h_b = h_o \left(\frac{p}{p_a}\right)^{\mu-1} \frac{|d^b|}{\langle d^b_{ref} - |d^b| \rangle} \tag{27}$$

where h_o is retained a user-defined positive constant, although it could also be made a function of the void ratio e (e.g. [19, 6]). Exponent μ is suggested to take values $0.5 \le \mu \le 1$. All simulations in this paper have been performed with $\mu = 1$, i.e. the value of the fixed μ in the respective equation of Papadimitriou et al. [27]. Furthermore, note that d^b_{ref} is a reference distance corresponding roughly to the θ-related 'diameter' of the bounding surface, which is given by:

$$d^b_{ref} = \sqrt{2/3}\left(\alpha^b_\theta + \alpha^b_{\theta+\pi}\right) \tag{28}$$

Given the plastic strain rate, one may specify the kinematic hardening rule of the proposed formulation, which is expressed via $d\boldsymbol{\alpha}$. This is attained by imposing the consistency condition $df = 0$, which gives:

$$d\boldsymbol{\alpha} = \langle \Lambda \rangle h_b h_f (\boldsymbol{\alpha}^b - \boldsymbol{\alpha}) \tag{29}$$

Finally, taking into account that $d\boldsymbol{\sigma} = d\mathbf{s} + dp\mathbf{I}$, Eqs. (7a), (7b), (8) and (24) can be rewritten in terms of the total strain rates $d\mathbf{e}$ and $d\varepsilon_p$, as:

$$d\boldsymbol{\sigma} = 2G_t\, d\mathbf{e} + K_t\, d\varepsilon_p \mathbf{I} - \langle \Lambda \rangle (2G_t \mathbf{n} + KD\mathbf{I}) \tag{30}$$

The first two terms of the right side of Eq. (30) correspond to an elastic prediction of the effective stress rate $d\boldsymbol{\sigma}$ and the third term to the plastic correction, which is necessary only when $\Lambda > 0$. In this case, the loading index Λ must also be rewritten in terms of $d\mathbf{e}$ and $d\varepsilon_p$. This is achieved by substituting Eqs. (11a)–(11c) into Eq. (9), which leads to:

$$\Lambda = \frac{2G_t \mathbf{n} : d\mathbf{e} + VK_t\, d\varepsilon_p}{K_p + 2G_t - VK_t D} \tag{31}$$

6. Effect of sand fabric evolution during cyclic shearing

Whenever fabric effects are accounted for in elastoplastic models, the resulting formulations are relatively complex, since they are usually characterized by either modified stress invariants [20], or by joint stress and plastic strain invariants [3]. The approach followed in this paper is much simpler: fabric evolution is assumed to merely affect the plastic strain rate $d\boldsymbol{\varepsilon}^p$, through an empirical factor h_f that scales the plastic modulus K_p in Eq. (26).

The formulation of h_f is based on a series of experimental observations that are fully described in Papadimitriou [26] and Papadimitriou et al. [27]. In summary, combined results from various laboratory studies of sand response show that successive shearing cycles of relatively small amplitude lead to a continuously stiffening unloading–reloading response [18]. Fabric evolution, namely changes in the orientation of contact normals, must be regarded as the governing factor of this response, since such continuously stiffening unloading–reloading behavior has been observed not only in drained shearing [18], but also in undrained shearing, at least far from initial liquefaction [9,31].

On the other hand, Ladd et al. [18] showed that when the successive shearing cycles are of larger amplitude, the unloading paths become significantly more compliant. In parallel, Ishihara et al. [15], based on experimental evidence such as that shown in Fig. 5, established that the unloading paths become compliant only when they initiate after dilation has occurred (e.g. compare unloading paths 6–7 and 8–9 to paths 2–3 and 4–5 in Fig. 5). In other words, they identified the phase transformation line (PTL), i.e. the stress threshold between contractive and dilative monotonic shearing, as the borderline between gradually stiffening and compliant unloading. This is in agreement with studies of fabric evolution, which show significant re-structuring of the fabric upon the onset of dilation [23].

Although fabric is a fully directional property, the previous experimental evidence allows for a simplifying simulation of its effect on the stress–strain behavior via scalar h_f in Eq. (26). In this model, h_f employs the use of

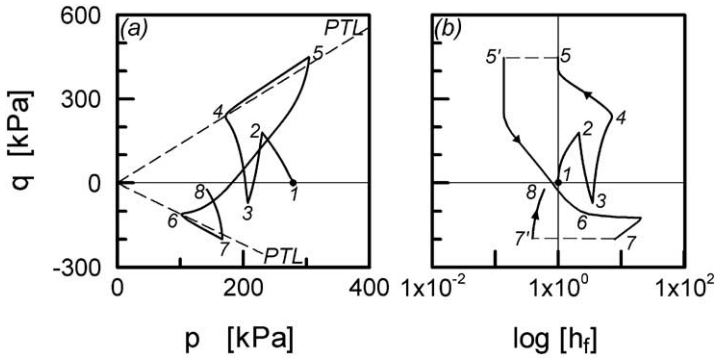

Fig. 6. Simulation of an undrained triaxial test including shear reversals: (a) effective stress path [q–p], (b) evolution of index h_f during this test.

a macroscopic second order fabric tensor $\mathbf{F}$, as:

$$h_f = \frac{1 + \langle \mathbf{F} : \mathbf{I} \rangle^2}{1 + \langle \mathbf{F} : \mathbf{n} \rangle} \tag{32}$$

If this fabric tensor $\mathbf{F}$ is deconvoluted according to:

$$\mathbf{F} = \mathbf{f} + (f_p/3)\mathbf{I} \tag{33}$$

where $f_p = \text{trace}(\mathbf{F})$, then Eq. (32) can be rewritten in terms of $\mathbf{f}$ and f_p as:

$$h_f = \frac{1 + \langle f_p \rangle^2}{1 + \langle \mathbf{f} : \mathbf{n} \rangle} \tag{34}$$

According to Eq. (34), when f_p increases, the value of h_f increases as well and leads to a smaller plastic strain rate (Eqs. (8), (9) and (26)). On the contrary, when $\mathbf{f}$:$\mathbf{n}$ increases, the opposite trend is observed. In all cases, scalar h_f takes merely positive values, due to the included Macauley brackets.

Based on the above, the role of $\mathbf{F}$ can be deconvoluted into the roles of f_p and $\mathbf{f}$, which are distinctly different. Similarly, the definition of rates $\mathrm{d}f_p$ and $\mathrm{d}\mathbf{f}$ are also given a distinctly different form. Their common ground is the correlation of fabric evolution to dilative or contractive behavior, and consequently to the plastic volumetric strain rate $\mathrm{d}\varepsilon_p^p$:

$$\mathrm{d}f_p = H\,\mathrm{d}\varepsilon_p^p \tag{35a}$$

$$\mathbf{df} = -\mathrm{H}\left\langle -d\varepsilon_p^p \right\rangle [C\mathbf{n} + \mathbf{f}] \tag{35b}$$

where H and C are model parameters. It is noted that the general form of Eq. (35b) was used by Dafalias and Manzari [5], and is elaborated on in the upcoming Dafalias and Manzari [6], in an attempt to apply a strictly deviatoric (i.e. $f_p = 0$) fabric effect on the dilatancy coefficient D, instead of both a deviatoric and a volumetric fabric effect on the plastic modulus K_p proposed herein. According to Eq. (35a), f_p develops during all paths characterized by $\mathrm{d}\varepsilon_p^p \neq 0$, i.e. f_p follows practically the whole shearing history of the sand. This is not the case for the deviatoric part $\mathbf{f}$, which develops only when $\mathrm{d}\varepsilon_p^p < 0$ due to the Macauley brackets included in Eq. (35b). In other words, $\mathbf{f}$ develops only during dilation and in the opposite sense relative to tensor $[C\mathbf{n} + \mathbf{f}]$. In this way, tensor $[C\mathbf{n} + \mathbf{f}]$, and consequently $\mathrm{d}\mathbf{f}$, will eventually become zero and remain as such until a potential change in the shearing direction (which would change the direction of $\mathbf{n}$). According to Eqs. (35a) and (35b), while parameter H controls the rate of f_p and $\mathbf{f}$ development, parameter C corresponds to the max norm of $\mathbf{f}$.

To clarify the operation of Eqs. (35a) and (35b) and the role of the fabric evolution index h_f in Eq. (34), Fig. 6a presents a simulation of an undrained triaxial test including shear reversals, that resembles that of Fig. 5. In parallel, Fig. 6b presents the evolution of index h_f all along the simulated path of Fig. 6a. Observe that while scalar h_f is generally a continuous function for shear paths below the PTL (e.g. 1–4), it may present 'jumps' at points where the shearing direction is reversed after dilation has occurred (e.g. from point 5 to 5′). The reason for this 'jump' is the activation of the denominator of h_f.

In more detail, all along a shear path that remains under the PTL (where $\mathrm{d}\varepsilon_p^p > 0$, e.g. path 1–4), trace f_p and thus the numerator of h_f increases. This trend is reversed during dilation, where $\mathrm{d}\varepsilon_p^p < 0$ (e.g. along path 4–5). Nevertheless, the numerator never takes values less than 1, because of the included Macauley brackets.

As alluded above, the denominator of h_f does not follow the whole shearing history. For example, all along shear path 1–4 that remains under the PTL (where $\mathrm{d}\varepsilon_p^p > 0$), tensor $\mathbf{f} = \mathbf{0}$ and the denominator remains equal to 1. When the shear path continues beyond the PTL (e.g. path 4–5), tensor $\mathbf{f}$ begins to develop. Nevertheless, the value of the denominator remains equal to 1 during this dilative shear path, because $\mathbf{f}$ develops in the opposite sense of $\mathbf{n}$ and thus $\langle \mathbf{f} : \mathbf{n} \rangle = 0$. The denominator becomes larger than 1, only after a shear reversal that follows a dilative path (e.g. at point 5′, following path 4–5). The value it takes corresponds to the value of $\mathbf{f}$ developed during the preceding dilative path and is maintained until the next shear reversal, or until tensor $\mathbf{f}$ starts developing towards a different direction (e.g. beyond the PTL in triaxial extension in Fig. 6).

Application of this formulation showed that C should be

Table 1
Model parameters: calibration, typical range and values for the cyclic shearing of Nevada sand

Parameter	Physical meaning	Calibration	Typical range	Nevada sand
$(e_{cs})_a$	Critical state Line location	Triaxial tests	0.72–0.90	0.809
λ	in the $[e-\ln p]$ space		0.01–0.03	0.022
M_c^c	Critical state strength in triaxial compression	Triaxial compression tests	1.20–1.37	1.25
M_e^c	Critical state strength in triaxial extension	Triaxial extension tests	0.86–1.0	0.90
B	Elastic shear modulus constant	G_{max} data	500–900	520
a_1	Non-linearity of elastic shear modulus	$G_s/G_{max}-\gamma_c$ data	0.45–0.85	0.67
γ_1	Strain limit of elastic modulus degradation	$G_s/G_{max}-\gamma_c$ data (correlation to γ_{tv})	0.65×10^{-4}–2.5×10^{-4}	2.5×10^{-4}
ν	Elastic Poisson's ratio	1D unloading path	0.2–0.4	0.31
k_c^b	Effect of ψ on peak stress ratio	Triaxial compression tests	0.5–4.0	1.45
k_c^d	Effect of ψ on stress ratio at phase transformation	Triaxial compression tests	0.1–3.0	0.3
A_o	Dilatancy constant	Triaxial tests	1.0–3.0	2.1
h_o	Plastic modulus constant	Triaxial tests	1000–10000	5000
H_o	Fabric index constant	Cyclic triaxial tests	50,000–100,000	68,000
ζ	Effect of major principal stress on fabric index	Cyclic triaxial tests	0.5–2.5	1.0

estimated by:

$$C = \max|f_p|^2 \tag{36}$$

In this way, the maximum value of the denominator becomes equal to $1 + \max|f_p|^2$ i.e. the maximum value ever retained by the numerator, and the use of the fabric evolution index h_f necessitates only the calibration of H. Refined simulations can be obtained if the value of H is correlated to initial conditions by:

$$H = H_o\left(\frac{\sigma_{1o}}{p_a}\right)^{-\zeta}\langle -\psi_o\rangle \tag{37}$$

where H_o and ζ are positive constants, ψ_o is the value of the state parameter at consolidation and σ_{1o} is the value of the major principal effective stress at consolidation. Based on Eq. (37), parameter H becomes non-zero merely for initially dilative states ($\psi_o < 0$). This implies that only for such states the effect of fabric evolution is considered necessary to be simulated. Similarly, the more dilative the state is, the more important should the effect of fabric evolution be. Hence, H is set to increase with increasing $\langle -\psi_o\rangle$, as well as with decreasing σ_{1o}. Furthermore, the use of σ_{1o} as a measure of the initial confinement in Eq. (37) was qualified over the mean stress p_o (utilized in the respective equation of Papadimitriou et al. [27]) for better simulation of the effect of initial stress anisotropy on the rate of fabric evolution.

The form of h_f in this paper is a generalization of a similar, but more simplified, fabric evolution index that was presented by Papadimitriou [26] and Papadimitriou et al. [27,28]. In those cases, the emphasis was on triaxial shearing and a non-directional index h_f in the form of a ratio of appropriate plastic volumetric strain integrals could be successfully used. In the multiaxial stress space, the directivity of fabric evolution should be accounted for and is incorporated here via the fabric tensor **F**. Nevertheless, all underlying assumptions for fabric evolution remain similar and so is the operation of a ratio-like index h_f as a scalar multiplier of the plastic modulus K_p.

7. Model evaluation

Table 1 presents the list of model parameters, along with their range for typical non-cohesive soils and comments regarding the calibration procedure. As deduced from this table, most parameters are calibrated on the basis of monotonic and cyclic triaxial tests, supplemented by resonant column tests. Details on the calibration procedure, as well as sensitivity runs, can be found in Ref. [27]. Only parameters H_o and ζ of this model are not included in Ref. [27] and this is because the fabric evolution index h_f has been formulated in a new way, herein. Nevertheless, these parameters are calibrated similar to F_o and χ of Ref. [27], which are the respective parameters related to h_f in that paper.

To evaluate the performance of the proposed model for multiaxial cyclic shearing under widely variable initial conditions, a total of 27 cyclic shearing tests are used. These include resonant column, triaxial and direct simple shear tests on Nevada sand [2], for two distinct initial void ratios: $e_o \cong 0.66$ and $e_o \cong 0.73$. All pertinent simulations are performed with the parameter values presented in Table 1. Similar comparisons for monotonic (drained and undrained) tests on the same sand are presented by Papadimitriou et al. [27].

Fig. 7 presents summary comparisons of model simulations to data for the secant shear modulus G_s and the hysteretic

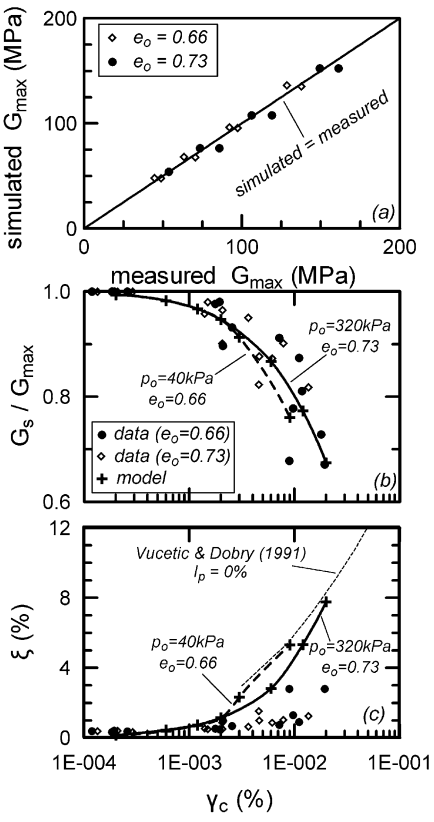

Fig. 7. Summary comparison of simulations versus data from 15 resonant column tests for Nevada sand [2], in terms of: (a) G_{max}, (b) $G_s/G_{max}-\gamma_c$ and (c) $\xi-\gamma_c$.

damping ξ taken from 15 resonant column tests, under various consolidation stresses ($p_o = 40$, 80, 160 and 320 kPa) and densities ($e_o \cong 0.66$ and 0.73). More specifically, in Fig. 7a, each symbol corresponds to a different test and is obtained using as coordinates on one hand the measured value, and on the other hand the respective simulated value of G_{max}. The solid diagonal line is the locus of perfect agreement between simulations and measurements. The notation in Fig. 7b and c and is not the same. More specifically, circular and rhombic symbols correspond to test data, while the dashed and solid lines denote average estimates of the upper and lower bounds of the simulated $G_s/G_{max}-\gamma_c$ and $\xi-\gamma_c$ curves for the initial conditions at hand. These estimates are based on example simulations marked by crosses in Fig. 7b and c.

It is deduced that the proposed model simulates the values of G_s accurately, from their initial values G_{max} (Fig. 7a) to their degraded values for larger cyclic shear strain amplitudes, expressed through the G_s/G_{max} ratios (Fig. 7b). On the other hand, the damping ratio ξ values are overestimated for cyclic strain amplitudes γ_c larger than about 3×10^{-5}. This overestimation can be attributed to the fact that the pertinent ξ measurements are relatively low compared with empirical curves for non-cohesive soils from the literature. For example, observe the pertinent curve of Vucetic and Dobry [33] added to Fig. 7c (thin dashed line).

Fig. 8 compares the measured to the simulated response in two element tests performed on Nevada sand. Specifically, plots 8a(i) and 8a(ii) present the measured effective stress path ($q-p$) and deviatoric stress–strain relation ($q-\varepsilon_v$) of a cyclic triaxial liquefaction test with $e_o \cong 0.73$, while plots 8a(iii) and 8a(iv) present their simulations. Similarly, plots 8b(i) and 8b(ii) present the measured $\tau-\sigma_v$ relation and the $\tau-\gamma$ relation of a cyclic direct simple shear liquefaction test with $e_o \cong 0.66$, while plots 8b(iii) and 8b(iv) present their simulations. It is observed that the proposed model simulates test measurements in an equally satisfactory manner, for both triaxial and direct simple shearing conditions.

For a more global evaluation of the simulation of excess pore pressure buildup, Fig. 9 presents a summary comparison of simulations to data from 12 cyclic liquefaction tests on Nevada sand. In particular, Fig. 9a refers to 6 triaxial liquefaction tests with $e_o \cong 0.73$, while Fig. 9b refers to 6 direct simple shear liquefaction tests with $e_o \cong 0.66$. Note that these results include the tests of Fig. 8 (tests 1 and 2), as denoted. The comparison is performed in terms of the rate of

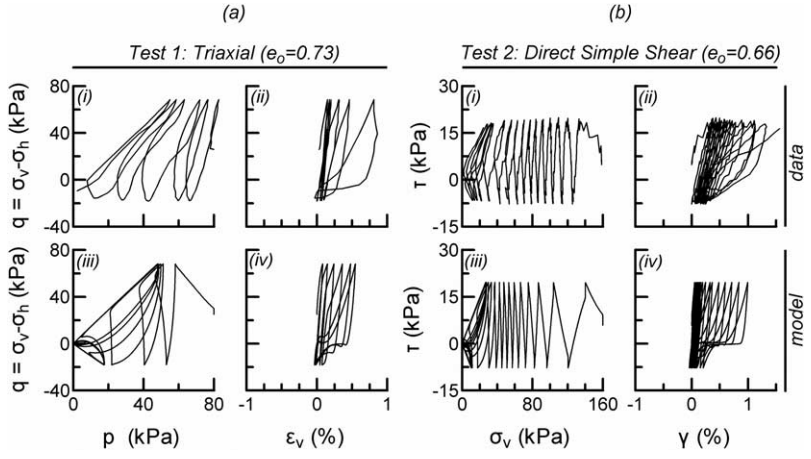

Fig. 8. Example comparisons of data versus simulations of 2 cyclic liquefaction tests on Nevada sand [2]: (a) triaxial test, (b) direct simple shear test.

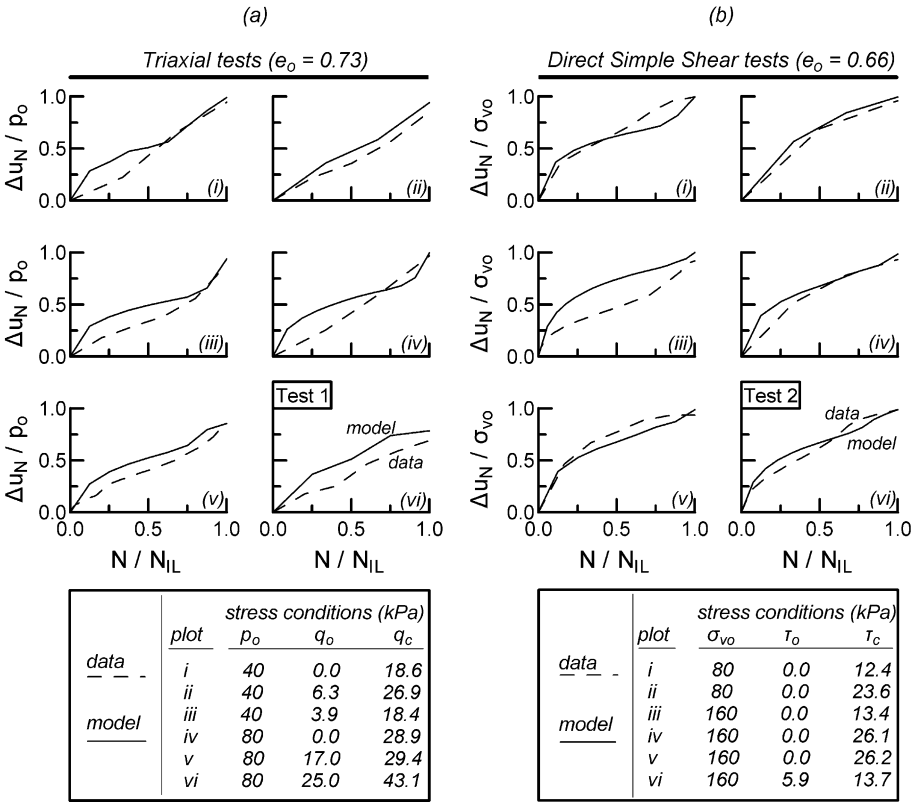

Fig. 9. Summary comparison of data versus simulations of 12 cyclic liquefaction tests on Nevada sand [2], in terms of the 'average' rate of excess pore pressure Δu_N with number of shear cycles N: (a) triaxial tests, (b) direct simple shear tests.

buildup of the 'average' excess pore pressure Δu_N versus the number of shear cycles N. The average excess pore pressure Δu_N corresponds to the value of Δu after the completion of N shearing cycles. To enable comparison between tests of different initial and shearing conditions, Δu_N is normalized to the p_o of each triaxial test and to the initial vertical consolidation stress σ_{v0} of each direct simple shear test. For the same reason, the number of shear cycles N is normalized to N_{IL}, i.e. the number of shear cycles to initial liquefaction. On the whole, simulations are in good gross agreement with experimental data, despite the variability of initial and shearing conditions that is noted in the legends of Fig. 9a and b.

Finally, of practical interest is the accuracy of the predicted liquefaction strength in both triaxial and direct simple shear testing conditions. This is evaluated in Fig. 10, in terms of the appropriate liquefaction curves: q_c/p_o–N_{IL} for triaxial tests (Fig. 10a) and τ_c/σ_{v0}–N_{IL} for direct simple shear tests (Fig. 10b). Observe that despite the considerable scatter of test results, the average liquefaction curves procuring from the simulations are in good agreement with the curves that are based on the test data, irrespective of initial and shearing conditions.

In order to ascertain the contribution of the constitutive ingredients introduced in this paper to the above successful model performance, some of the simulations are repeated by neglecting:

(a) the Ramberg–Osgood type formulation (by setting

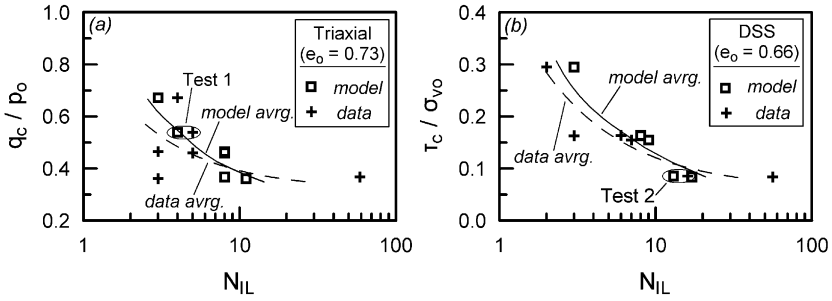

Fig. 10. Summary comparison of data versus simulations of 12 cyclic liquefaction tests on Nevada sand [2], in terms of the number of cycles N_{IL} for initial liquefaction: (a) triaxial tests, (b) direct simple shear tests.

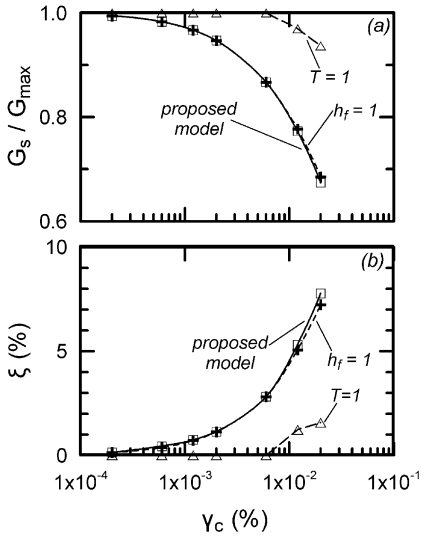

Fig. 11. Parametric simulations of resonant column tests, in terms of the average: (a) $G_s/G_{max}-\gamma_c$ curves and (b) $\xi-\gamma_c$ curves. Squares: proposed model runs; triangles: runs neglecting the Ramberg–Osgood type formulation ($T = 1$); crosses: runs neglecting the effect of fabric evolution ($h_f = 1$).

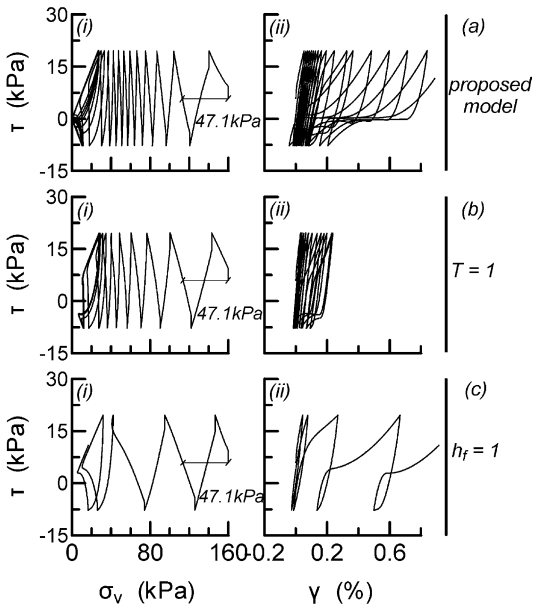

Fig. 12. Parametric simulations of a cyclic direct simple shear test, in terms of the $\tau-\sigma_v$ and the $\tau-\gamma$ relations: (a) proposed model run, (b) run neglecting the Ramberg–Osgood type formulation ($T = 1$) and (c) run neglecting the effect of fabric evolution ($h_f = 1$).

$a_1 = 1.0$, that leads to $T = 1$) and
(b) the effect of fabric evolution (by setting $H_o = 0$, that leads to $h_f = 1$).

More specifically, Fig. 11 refers to the resonant column test simulations for $p_o = 320$ kPa and $e_o = 0.73$ of Fig. 7, and compares the new simulations to those obtained with the parameters of Table 1, in terms of the average curves of $G_s/G_{max}-\gamma_c$ and $\xi-\gamma_c$. The curves referring to runs performed with the parameters of Table 1 are denoted by 'proposed model', while the curves referring to the two sets of parametric runs by '$T = 1$' and '$h_f = 1$,' accordingly. Similarly, Fig. 12 refers to the direct simple shear cyclic liquefaction test 2 of Fig. 8b, and presents an analogous comparison of the three simulations by maintaining the same notation. To attain a fair comparison between the three sets of simulations, the value of the plastic modulus constant h_o in the '$T = 1$' and '$h_f = 1$' parametric runs has been appropriately increased to $h_o = 10\,000$ and $h_o = 8000$, respectively, in order to achieve the same value of excess pore pressure $\Delta u (= 47.1$ kPa) after the first shear cycle in all three simulations (Fig. 12).

Observe that neglecting the effect of fabric evolution ('$h_f = 1$') in Fig. 11 produces minute differences in the simulated response. On the other hand, when the Ramberg–Osgood type formulation is neglected ('$T = 1$'), the model cannot simulate the non-linearity involved in the response of non-cohesive soils at relatively small cyclic strain amplitudes (compare with actual measurements in Fig. 7b and c).

In the parametric analyses of Fig. 12, it becomes evident that neglecting the effect of fabric evolution ('$h_f = 1$'), initial liquefaction is reached faster, due to an unrealistically high rate of excess pore pressure buildup (compare with actual measurements in Fig. 8b). Furthermore, the rate of permanent strain accumulation is also overestimated (compare with actual measurements in Fig. 8b). On the other hand, neglecting the Ramberg–Osgood type formulation does not produce a large differentiation in the simulated response, with the exception of the relatively smaller strains.

8. Conclusions

In summary, this paper proposes a new kinematic hardening, yield/bounding surface plasticity model for multiaxial cyclic shearing of sands. The model incorporates strength anisotropy, to the extent that the proposed shape of the non-circular conical surfaces in the multiaxial stress space is formulated in accordance with experimental evidence. The state of the material cannot be determined by the current $\boldsymbol{\sigma}$, but also requires the current location of the yield surface $\boldsymbol{\alpha}$. Moreover, shearing memory is one of the basic constitutive ingredients and is introduced via: (a) a non-linear hysteretic (Ramberg–Osgood type) formulation for the elastic strain rate $d\boldsymbol{\varepsilon}^e$ and (b) an empirical estimator of the effect of fabric evolution during shearing, which affects the plastic strain rate $d\boldsymbol{\varepsilon}^p$. These are the two basic novelties of the proposed model.

The comparison of analytical simulations to experimental data verifies that the model can provide satisfactory accuracy for multiaxial cyclic shearing, under variable initial stresses and densities and shear strain amplitudes ranging from 1×10^{-6} up to 1×10^{-2}, i.e. from low amplitude

resonant column tests to the final stages of cyclic liquefaction tests (at initial liquefaction).

Of special importance is that this accuracy is obtained with a single set of parameters, due to the aforementioned two basic novelties of the proposed model. In particular, it is the Ramberg–Osgood type formulation that is crucial for simulating the non-linear hysteretic response at relatively small cyclic strain amplitudes, a key element of behavior in wave propagation problems. In addition, it is the fabric evolution index h_f that ensures accuracy in the simulation of liquefaction and cyclic mobility problems, encountered for relatively large cyclic shear strains.

This accuracy has been the primary aim of this research, since it is considered as the key element for consistent numerical analyses of boundary value problems of geotechnical earthquake engineering. Indeed, such analyses require the simultaneous modeling of seismic wave propagation through the soil mass, concurrently with the resulting excess pore pressure buildup, strain accumulation and shear strength degradation.

It is acknowledged that the implementation of the proposed model in a numerical code may lead to certain modifications in the mathematics of constitutive equations, as a result of verifying the performance of the model for more complex shearing and boundary conditions. Nevertheless, the concepts, assumptions and basic equations of the proposed model are not expected to require modifications.

Acknowledgements

The financial support of the first author by the State Fund Institution of Greece (I.K.Y.) is gratefully acknowledged. In addition, both authors would like to sincerely thank Professor Y.F. Dafalias for his advice and guidance during the long course of model development.

References

[1] Argyris JH, Faust G, Szimmat J, Warnke P, William K. Recent developments in finite element analyses of prestressed concrete reactor vessels. Nuclear Engineering and Design 1974;28:42–75.

[2] Arulmoli K, Muraleetharan KK, Hossain MM, Fruth LS. VELACS: verification of liquefaction analyses by centrifuge studies; Laboratory Testing Program—Soil Data Report. Research Report, The Earth Technology Corporation, 1992.

[3] Baker R, Desai CS. Induced anisotropy during plastic straining. Int J Numer Anal Meth Geomech 1984;8:167–85.

[4] Been K, Jefferies MG. A state parameter for sands. Geotechnique 1985;35(2):99–112.

[5] Dafalias YF, Manzari M. Modeling of fabric effect on the cyclic loading response of granular soils. Proceedings of the 13th ASCE Engineering Mechanics Specialty Conference, Baltimore, 1999 (in CD-ROM).

[6] Dafalias YF, Manzari M. A simple plasticity sand model accounting for fabric change effects. J Geotech Geoenviron Engng, ASCE, 2001. To appear.

[7] Dafalias YF, Popov EP. A model of nonlinearly hardening materials for complex loadings. Acta Mechanica 1975;21:173–92.

[8] Dobry R, Vucetic M. State-of-the-art report: dynamic properties and response of soft clays deposits. Proceedings of the International Symposium on Geotechnical Engineering of Soft Soils, Mexico City, 2, 1987. p. 51–87.

[9] Egglezos DN, Bouckovalas GD. Permanent strain and pore pressure relations for cyclic loading of sand. Proceedings of the Second International Conference on Earthquake Geotechnical Engineering, Lisbon, 1, 1999. p. 131–6.

[10] Gajo A, Wood DM. A kinematic hardening constitutive model for sands: the multiaxial formulation. Int J Numer Anal Meth Geomech 1999;23:925–65.

[11] Ghaboussi J, Momen H. Modelling and analysis of cyclic behaviour of sands. In: Pande GN, Zienkiewicz OC, editors. Soil mechanics—transient and cyclic loads, New York: Wiley, 1982.

[12] Hardin BO. The nature of stress–strain behavior of soils, State-of-the-art report. Proceedings of the ASCE Specialty Conference on Earthquake Engineering and Soil Dynamics, Pasadena, 1978. p. 3–90.

[13] Hueckel T, Nova R. Some hysteresis effects of the behavior of geological media. Int J Solids Struct 1979;15:625–42.

[14] Ishihara K. Evaluation of soil properties for use in earthquake response analysis (invited lecture). In: Dingar R, Pande GN, Studer JA, editors. International symposium on numerical models in geomechanics, Zurich, Rotterdam: A.A. Balkema, 1982. p. 237–59.

[15] Ishihara K, Tatsuoka F, Yasuda S. Undrained deformation and liquefaction of sand under cyclic stresses. Soils Foundations 1975;15(1): 29–44.

[16] Jefferies MG. Nor-sand: a simple critical state model for sand. Geotechnique 1993;43(1):91–103.

[17] Lade PV, Duncan JM. Elastoplastic stress–strain theory for cohesionless soil. J Soil Mech Found Div, ASCE 1975;101(10):1037–53.

[18] Ladd CC, Foott R, Ishihara K, Schlosser F, Poulos HG. Stress-deformation and strength characteristics, State-of-the-art report. Proceedings of the Ninth International Conference on Soil Mechanics and Foundation Engineering, Tokyo, 2, 1977. p. 421–94.

[19] Li XS, Dafalias YF. Dilatancy for cohesionless soils. Geotechnique 2000;50(4):449–60.

[20] Liang RY, Shaw H-L. Anisotropic hardening plasticity model for sands. J Geotech Engng, ASCE 1991;117(6):913–33.

[21] Manzari MT, Dafalias YF. A critical state two-surface plasticity model for sands. Geotechnique 1997;47(2):255–72.

[22] Matsuoka H, Nakai T. Stress-deformation and strength characteristics of soil under three different principal stresses. Proceedings of the Japanese Society of Civil Engineering, 232, 1974. p. 59–70.

[23] Nemat-Nasser S, Tobita Y. Influence of fabric on liquefaction and densification potential of cohesionless sand. Mech Mater 1982;1:43–62.

[24] Mroz Z, Norris VA, Zienkiewicz OC. An anisotropic hardening model for soils and its application to cyclic loading. Int J Numer Anal Meth Geomech 1978;2:203–21.

[25] Nova R, Wood DM. A constitutive model for sands in triaxial compression. Int J Numer Anal Meth Geomech 1979;3:255–78.

[26] Papadimitriou AG. Elastoplastic modeling of monotonic and dynamic behavior of soils. Doctorate Thesis, Department of Geotechnical Engineering, Faculty of Civil Engineering, National Technical University of Athens, June 1999 (in Greek).

[27] Papadimitriou AG, Bouckovalas GD, Dafalias YF. Plasticity model for sand under small and large cyclic strains. J Geotech Geoenviron Engng, ASCE 2001;127(11):973–83.

[28] Papadimitriou AG, Bouckovalas GD, Dafalias YF. Use of elastoplasticity to simulate cyclic sand behavior. Proceedings of the Second International Conference on Earthquake Geotechnical Engineering. Lisbon, 1, 1999. p. 125–30.

[29] Ramberg W, Osgood WR. Description of stress–strain curve by three parameters. Technical Note 902, National Advisory Committee for Aeronautics, Washington, DC, 1943.

[30] Rowe PW. The stress–dilatancy relation for static equilibrium of an assembly of particles in contact. Proc R Soc 1962;269A:500–27.

[31] Seed HB, Booker JR. Stabilization of potentially liquefiable sand deposits using gravel drains. J Geotech Engng Div, ASCE 1977;103(7):755–68.
[32] Vucetic M. Cyclic threshold shear strains in soils. J Geotech Engng, ASCE 1994;120(12):2208–28.
[33] Vucetic M, Dobry R. Effect of soil plasticity on cyclic response. J Geotech Engng, ASCE 1991;117(1):89–107.
[34] Wood DM, Belkheir K, Liu DF. Strain softening and state parameter for sand modelling. Geotechnique 1994;44(2):335–9.